Dynamical systems techniques for enhancing microfluidic mixing

Sanjeeva Balasuriya

School of Mathematical Sciences, University of Adelaide, Adelaide SA 5005, Australia

E-mail: sanjeevabalasuriya@yahoo.com

17 March 2015

Abstract.

Achieving rapid mixing is often desirable in microfluidic devices, for example in improving reation rates in biotechnological assays. Enhancing mixing within a particular context is often achieved by introducing problem-specific strategies such as grooved or twisted channels, ac electromagnetic fields or oscillatory microsyringe flows. Evaluating the efficiency of these methods is challenging since either experimental fabrication and sensing, or computationally expensive direct numerical simulations with complicated boundary conditions, are required. A review of how mixing can be quantified when velocity fields have been obtained from such situations is presented.

A less-known alternative to these methods is offered by dynamical systems, which characterizes the motion of collective fluid parcel trajectories by studying crucial interior flow barriers which move unsteadily, but nevertheless strongly govern mixing possibilities. The methodology behind defining these barriers and quantifying the fluid transport influenced by them is explained. Their application towards several microfluidic situations (e.g., best cross-flow positioning in cross-channel micromixers, usage of channel curvature to enhance mixing within microdroplets traveling in a channel, optimum frequencies of velocity agitations to use) is discussed.

Keywords: dynamical systems, microfluidic, fluid interface, fluid transport, optimization, microdroplet Submitted to: *J. Micromech. Microeng.*

1. Introduction

As microfluidic devices become increasingly relevant in today's biotechnological revolution, an inescapable physical fact is that flow in such devices are typically *of low Reynolds number* [1–5]. This occurs because the spatial lengthscale L, and the typical speed U are both small, and whatever the kinematic viscosity happens to be, the Reynolds number $\mathrm{Re} := UL/\nu$ is inevitably small. The end result is that microfluidic flows behave similarly to flows of highly viscous fluids, and in particular the absence of turbulence (i.e., high Re flow) makes the flows very regular, or *laminar* [5]. Indeed, the *Stokes limit* of infinite Re is sometimes used for modeling such flows [6–14]. The laminar nature of the flow is unfortunate in many applications in which excellent mixing is required, for example in mixing together a sample and a reagent for a biomedical assay. It is desirable in such situations to mix the fluids quickly, to account for fast chemical kinetics. Diffusion does act to mix fluids, but in typical microfluidic applications occurs on a time-scale that is too slow to be efficient *in and of itself* [1, 5].

1.1. Advective mechanisms for microfluidic transport

Dynamical systems offers an approach to tackle this difficulty, based on the observation by Aref [2] that it is possible to obtain complicated mixing in fluids in which the Eulerian velocity field is completely regular. This mixing is often loosely referred to as *chaotic mixing*, which is a purely advective mechanism in which nearby fluid particles lose sight of one another as time progresses, or equivalently a particle's eventual trajectory depends highly sensitively on its initial position. It is instructive to note that chaotic mixing *cannot* occur in two-dimensional (2D) flows which are steady because of the Poincaré-Bendixson theorem [15, 16], nor in three-dimensional (3D) steady inviscid flows in which the velocity and vorticity are linearly independent [17, 18]. This allows for the possibility of chaotic mixing in 2D *unsteady* flows, or in 3D *viscous* and/or *unsteady* flows—situations which can be used to advantage to enhance microfluidic mixing.

Two schematics of microfluidic situations in which mixing might be desired are shown in Figure 1. Figure 1(a) shows two different fluids being introduced into a channel on the left; the typical behavior is for them to flow along the channel, forming an interface along the middle of the channel (magenta line) across which they tend not to mix [5, 19–35]. This phenomenon has been amply demonstrated both experimentally and theoretically. Figure 1(b) shows a streamline pattern associated with a microdroplet traveling along a channel [36–43], in the frame of reference of the microdroplet. In typical applications the exterior (carrier) fluid is immiscible, with the microdroplet carrying within it two cells containing different fluids, as demarcated by the interior magenta line. These cells arise from the formation process of the microdroplet; the two fluids are injected in to the channel at the same location, and the hope is that they mix within the microdroplet rapidly to improve the chemical reaction rate between the two fluids. This configuration is also extensively studied in the experimental [36, 38, 39, 41–46] and theoretical [7–9, 14, 40, 47, 48] microfluidics literature. It should be highlighted that the methods that are to be discussed in this article are *not* confined to the two pictures shown in Figure 1; these are prototypical examples drawn from microfluidics which will be used to illustrate how the techniques can be used.

While the pictures in Figure 1 show idealized steady conditions in which mixing between the two relevant fluids does *not* occur, the concept of chaotic mixing can be used to make it occur. That is, if it were possible using some mechanism to create an *additional* fluid velocity which conforms with the necessary conditions for chaotic mixing, then fluid interchange might be achieved. For the 2D situations, a time-variation would be *necessary* to generate chaotic transport; such time-variation would also be advantageous in 3D. In practical situations, time-variation in the velocity can be achieved in a couple of ways: by an *active* method, or a *passive* method.

Active methods are those which supply an energy to the system. These include for example pumping fluid back and forth (for example in the transverse direction to the channel flow in Figure 1) using syringes or cross-channels [31, 32, 35, 49–55], vibrating boundary membranes to generate an additional interior flow velocity [51, 52], or applying external oscillating electromagnetic fields to influence charged particles within the fluid [25, 28, 30, 56–60]. These methods will cause fluctuating velocities in the frame of reference of the flow barriers, thereby engendering transport across them. Typically, the fluctuations are

oscillatory in time, for example sinusoidal, which is of course natural for fluctuations driven by alternating currents. In situations such as this, one might seek the 'best' strategy to optimize transport. For example, prompted by experimental [25, 28, 29, 35, 56, 61–68] computational [30, 62–64, 66, 69] and theoretical [70] evidence on the *presence* of an optimal frequency of oscillation, one might develop methodology to *find* this particular frequency [71]. Alternatively, one might analyze the locations at which to position microsyringes or insert cross-channels [33, 34, 72], in order to maximize transport. These problems can be tackled using the dynamical systems theory that is explained in this article, and a description appears in Sections 5.1 and 5.2.

Passive methods are those which do not supply energy, but use passive mechanisms which help to cause the required velocity agitations. They take advantage of physical/chemical phenomena such as gravity, capillary action, surface tension or osmosis. The simplest of these approaches is to have bends or curves in microchannels to passively generate anomalous velocities [8, 9, 14, 19–22, 38, 73]. Even if the flow in the curved channel remains steady, this can cause *unsteady* flows across flow barriers, which as has been discussed is important in generating transport. To see why this is so, imagine a microdroplet such as that pictured in Figure 1(b)) traveling along a curved channel. When viewed *in the frame of reference of the droplet*, the flow barrier inside the droplet is experiencing different velocities as it traverses different curves in the channel. Hence the flow across the flow barriers would be unsteady. There are many examples in the literature which indicate that traveling within curved channels does indeed engender transport within cells in a microdroplet [8, 11, 37, 37–39, 39, 74–77]. Another passive approach which has been studied is having *grooves* in a channel [20, 24, 26, 78, 79], which once again will cause velocity agitations. As in the active approach, one might ask questions on how best to apply the passive strategy (i.e., how to bend the channels, or where to put the grooves) in order to optimize the particular mixing that one is seeking; this is discussed in Section 5.3.

1.2. Diffusive mixing

An important aspect absent from the discussion so far is the role of *diffusion*. Indeed, in some areas of fluid mechanics the above advective mechanisms, i.e., variations in the Eulerian velocity field of the fluid driving Lagrangian fluid particle trajectories, is defined as *stirring*, whereas *mixing* explicitly means the process of diffusion. Since diffusion occurs at slow rates in microfluidic devices, using this specific 'definition' of mixing as pure diffusion is somewhat limited in the present context. As has been argued, unsteady advection (i.e., stirring) is *essential* to achieve fluid transport across the flow barriers in (inevitably low Re number) microfluidic flows. But does this by itself *mix* the fluids together? The answer is that mixing can be achieved by diffusion acting *on top of* a judiciously chosen advective mechanism. Diffusive mixing can be made effective if there are *sufficiently small* blobs of one fluid immersed in a region of the other fluids; when the length-scale of these blobs reaches the diffusive length-scales, these blobs diffusive into the outer fluid, resulting in good *mixing* (in any sense of the word). If the blobs are too big, diffusive mixing is inefficient. Therefore a reasonable approach is to use advective mechanics, such as chaotic mixing, to help the fluid create sufficiently small blobs. A particularly efficient configuration of these blobs is if they are thin elongated elements, i.e.., filaments, with their widths smaller than the diffusive length-scale. Diffusion would then break them up, and the filament would mix into the surrounding fluid quickly.

To summarize the above discussion: good mixing in microfluidic devices requires a two-step process.

(i) A carefully chosen *unsteady* advective mechanism needs to be selected; this is essential in combating the laminar nature of the flow, and attempting to promote advective transport (such as chaotic mixing);

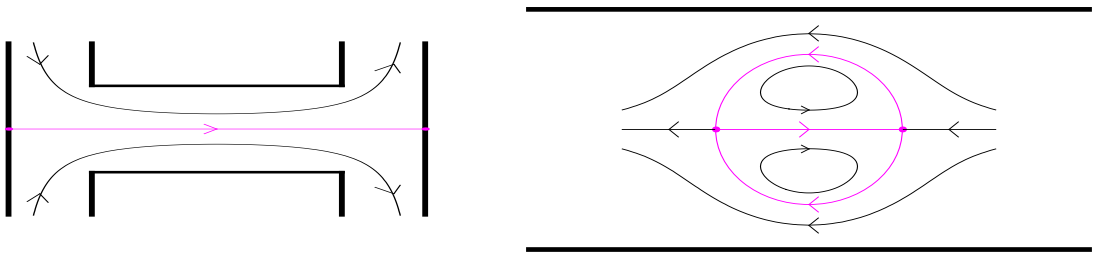

(a) (b)

Figure 1. Idealized steady microfluidic flows with flow barriers (magenta): (a) two fluids flowing along a channel, and (b) a two-cell microdroplet in a channel.

(ii) The advective strategy should result in fluid blobs or filaments, whose shapes are such that diffusive mixing is accelerated.

Thus, one can think of mixing as occuring via an *advection-driven diffusion* process [80]. This is often modeled in the literature using advection-diffusion equations [6, 81–83].

1.3. Optimizing mixing

Each microfluidic device being designed usually has a specific goal. Obtaining excellent mixing according to a device-dependent specification may be an important aspect in the design process. If so, it is necessary to fabricate the device such that the above two-step *advection-enhanced diffusive mixing* is maximized.

But how can one optimize this? The most obvious thing to do is to fabricate many devices with slightly different configurations, *experimentally* test the mixing in each, and choose the design which gives the best mixing. For the moment let us postpone the issue of how one might *measure* this mixing which is necessary for the comparison. This is difficult in experimental microfluidic devices, since ultra-high resolutions for the measurement method (e.g., *particle image velocimetry*, or PIV) will be needed. If we are able to do obtain these measurements, and do this comparison across the devices, a particular design could be chosen from among the experimental devices that we have fabricated, as the optimal one. This process is *ad hoc* at best since, realistically, only a small number of devices can be fabricated because of the considerable time and cost of the process. Usually, most laboratories will design and fabricate just *one* device at a time, and report on its performance in the literature [19, 22, 25, 28, 30, 35, 36, 38, 39, 41–46, 49, 61, 73]. This by itself offers only an incremental step in the understanding of design *optimization*, since comparison across many such designs is essential before any claim on optimized mixing can be made. The fact that the mixing measures used for devices manufactured at different laboratories are usually *different* [8, 12, 14, 39, 41–43, 76] exacerbates the difficulty of comparison. Experimentally determining the best designs to optimize mixing is therefore difficult, impractical and costly.

A cheaper alternative would be to first use *direct numerical simulations* (DNSs) of a particular design. In this approach, the relevant fluid equations (Navier-Stokes equations, or suitable simplifications such as the Stokes equations which characterize extremely low Reynolds number flows) need to be numerically solved using computational fluid dynamics (CFD). A significant difficulty in this process is how one expresses the necessary boundary conditions for the governing partial differential equations. The interfaces between fluids at which conditions need to be specified are themselves moving and changing shape, resulting in the necessity of expressing boundary conditions on moving interfaces, with this motion itself influencing the flow. As a result of this, most microfluidics-inspired DNSs available in the literature limit themselves to highly simplified geometries or idealized interface/boundary conditions [13, 14, 20, 21, 24, 25, 73, 76, 77, 84, 85]. The result of the DNS is the knowledge of the fluid velocity on a spatial and temporal grid, which can then be used for evaluating mixing. Emerging advances in computational techniques such as the immersed interface method [86, 87] might in the future help include the interior flow interfaces in a more realistic way. At this point, however, each DNS that is run needs to be carefully developed for each specific design. As in the experimental literature, DNS results are also usually reported for one specific design at a time [13, 14, 20, 21, 24, 25, 73, 76, 77, 84, 85], making comparisons of mixing efficiency once again difficult.

As a result of these considerable difficulties in either experimental or DNS microfluidic mixing evaluations, an approach which utilizes *simple models* has been proposed. Here, one expresses the fluid velocities in the device based on some kinematically- or dynamically-plausible hypothesis [7–11, 40, 88, 89]. Typically, the fluid velocities can be specified exactly, doing away with the need for DNS or PIV, but of course the velocities are based on highly-idealized models. While this is the least realistic of the three approaches, it offers the opportunity to quickly test across different configurations. For example, parameters such as the curvature of a channel bend, the location of a cross-channel, the frequency at which a microsyringe pushes fluid in, or the viscosity ratio between the fluids interior to an exterior from a droplet, can be manipulated quickly. A strong recommendation for these simple models is that they can be used as the basis for preliminary investigation, and suggstions for the 'best' parameter values can emerge from these analyses. This can enable an *informed* choice of parameters to investigate in proceeding to the more realistic, but more costly, DNS and experimental approaches.

Typically, it is the *fluid velocity* which is obtained through an experimental, DNS, or simple model approach, and the issue postponed in the discussion was how this can be used to *measure the mixing*. Section 2 has a discussion on dynamical systems methods which can be utilized to measure mixing in a global sense. However, as in the schematics of Figure 1, the goal may not be to have excellent global mixing, but rather to have excellent mixing *across the interface between the fluids*. Indeed, one might argue that the first step in achieving global mixing (if

that is the goal) is to promote mixing across the fluid interface(s). While in the idealized steady pictures in Figure 1 the interfaces are easy to explain, realistic microfluidic flows are *unsteady*, and even defining what the relevant fluid interfaces are becomes problematic. Thus, it is necessary to understand *flow barriers*, across which mixing is suppressed in *unsteady* situations. (It is the transport across these barriers that is to be assessed in the experimental devices.) Section 3 offers a discussion on how one might *determine* these flow barriers, concerning which there is a large and growing literature in dynamical systems. The issue of *quantifying* transport across these barriers is itself tricky, and explained in Section 4. Finally, Section 5 describes some recent successes of these dynamical systems methods for maximizing mixing (including new comparisons with experiments), and postulates other situations in which they have promise.

2. Measuring global mixing

Suppose that the time-varying velocity field $\boldsymbol{v}(\boldsymbol{x}, t)$ within a microfluidic device have been obtained by one of the three methods discussed previously: from an experimental device, from a DNS, or from a simple model. Then, the fluid trajectories are given by the solutions of the ordinary differential equation

$$\frac{d\boldsymbol{x}}{dt} = \boldsymbol{v}\left(\boldsymbol{x}, t\right) . \tag{1}$$

Equation (1) is the *advection equation* of the fluid, representing the simple fact that the rate of change of position of each fluid particle is given by its velocity. Suppose we imagine seeding particles across the spatial domain at an initial time (say, $t = 0$). Choose a specific particle which is at the location $\boldsymbol{x}_0$ at this time. Its Lagrangian trajectory $\boldsymbol{x}(t)$ is then the solution to (1), subject to the initial condition $\boldsymbol{x}(0) = \boldsymbol{x}_0$. By solving (1), numerically or otherwise, over many initial conditions, the Lagrangian trajectories of many particles in the fluid can be determined.

In realistic situations, $\boldsymbol{v}$ will only be known on a spatial grid, at discrete points in time. Knowing $\boldsymbol{v}$ by itself does *not* tell us about mixing; this velocity field information needs to be processed in some way to obtain mixing measures. Typically, the mixing measures will be changing with time t. Some possible approaches for obtaining these mixing measures are now discussed; a more extensive collection of mixing measures is available in review articles [82, 90].

2.1. Concentration variance: particle-based advection

A simplest way of quantifying mixing is to assume that each particle has a signature which is conserved as it moves around in the flow. For example if there are two fluids whose mixing together is to be assessed, one can assume that particles from one fluid are labeled '0' and those of the other fluid are labeled '1.' A finite number of particles is identified at time 0, and then their location at a general time t is determined by numerically solving (1). To see how the '0' and '1' particles have intermingled by this stage, the spatial domain is gridded into small boxes B_i, and the number of each particle type within each box is counted [81, 91, e.g.]. If $c_i(t)$ is the fraction of particle type '1' in box B_i at time t, the level of homogenization can be assessed by determining how uniform c_i is across all the boxes. A measure of this could be a standard variance

$$\sigma_v(t) := \left\langle \left| c_i - \langle c_i \rangle \right|^2 \right\rangle = \left\langle c_i^2 \right\rangle - \left\langle c_i \right\rangle^2 , \tag{2}$$

where $\langle \cdot \rangle$ represents the average over all the boxes. Since the c_i here are proxies for the spatial distribution of the concentration of particle '1,' (2) is a *concentration-variance* measure for mixing. Indeed, (2) is equivalent to the *segregation measures* suggested by Danckwerts in 1952 [92]. Expressions equivalent to (2) are often used in the literature to measure microfluidic mixing [8, 12, 14, 20, 22, 24, 25, 27, 30, 35, 41, 43, 73, 76, 77, 79], where the c_is can be obtained from some other means (see Section 2.2, for example) rather than particle advection. For example, the so-called *mixing measure* [19, 20, 22, 27, 27, 35] is effectively $1 - \sigma_v(t)$. In some experiments, the quantity c_i could have been estimated by optical methods (for example the pixel intensity associated with the presence of a dye [26, 30, 35, 61, 73]).

One shortcoming of using the particle-advected method for evolving the quantity c_i is that, since one merely uses the velocity field to directly push particles each with a fixed signature value (i.e., type '0' or type '1'), the effect of *diffusion* is not explicitly included in this approach.

2.2. Concentration variance: passively advected field

Rather than counting particles to estimate a concentration, a mathematically more precise method which also incorporates diffusion would be to think of an initial concentration of some quantity at time 0 as a quantity per unit volume entity, i.e., a density. For example, $c(\boldsymbol{x}, 0)$ could be the density distribution of a salt or dye at time 0, which might be high on one side of the microfluidic device and zero on another, because the dye is initially contained in one fluid and not the other. When quantifying 'mixing' now, the idea is to see how the dye mixes as time progresses, under the condition that there is a velocity field $\boldsymbol{v}(\boldsymbol{x}, t)$ acting on the fluid in the device. The evolution of the concentration $c(\boldsymbol{x}, t)$ is then governed by an advection-diffusion

equation [6, 81–83]

$$\frac{\partial c}{\partial t} + \boldsymbol{v}(\boldsymbol{x},t)\cdot\boldsymbol{\nabla} c(\boldsymbol{x},t) = \kappa\nabla^2 c(\boldsymbol{x},t) \tag{3}$$

where $\kappa \geq 0$ is a small diffusion coefficient. If in nondimensionalized form, κ in (3) can be thought of as the reciprocal of the Péclet number (which measures the relative importance of advective versus diffusive transport). Diffusion as represented by the Laplacian operator on the right-hand side of (3) is the averaged effect of small scale random (Gaussian) particle motions, which is well-known to be tiny in comparison to advective motion in microfluidic devices. Thus, (3) may be thought of as the modeling equivalent of a standard scenario used in microfluidic experiments: taking optical measurements to capture the spread of a dye [10, 38, 39, 43, 79].

Returning to the model (3), suppose an initial concentration distribution is given, and knowledge of the velocity $\boldsymbol{v}$ (gleaned from PIV, DNS, or a simple model) is available. Then, it is possible to numerically evolve the scalar field c using the equation (3) which is linear in the unknown, c. Having done so until a time t, it seems reasonable that one can then use (2) as a measure of mixing, where the averaging of c is performed over the spatial domain in any fashion (not necessarily by choosing a collection B_i of boxes).

However, this process has a significant practical problem, as argued by Thiffeault [82]. At tiny κ as appropriate to microfluidics, concentration gradients occur on length-scales of order $\kappa^{1/2}$. Thus any numerical scheme used in evolving c in (3), and any procedure used to determine the velocity field $\boldsymbol{v}$, should both be able to resolve to this tiny length-scale. While there are many studies which do use (3) to numerically compute concentration variances in this way, the validity of such results is perhaps questionable unless it is clear that a resolution of better than $\kappa^{1/2}$ is used.

2.3. Capturing multiscale behavior: mix-norms

Using $\kappa = 0$ in (3) means that the quantity c is conserved by fluid particles when following the flow, since for any trajectory $\boldsymbol{x}(t)$ which obeys (1), the material derivative

$$\frac{D}{Dt}\left[c\left(\boldsymbol{x}(t),t\right)\right] = \frac{\partial c}{\partial t} + \frac{d\boldsymbol{x}}{dt}\cdot\boldsymbol{\nabla} c(\boldsymbol{x},t) = 0$$

by using (3) with $\kappa = 0$. (It should be noted however that (3) in the *limit* $\kappa \to 0$ does *not* give the same results as one gets by setting $\kappa = 0$. This is for the same reason that high Reynolds numbers flows are quite different from inviscid ones; the behaviour as $\mathrm{Re} \to \infty$ is not the same as for $\mathrm{Re} = \infty$.) In this $\kappa = 0$ situation, it can also be shown that the variance of c does not change with time [82, 93], rendering useless its role as a mixing measure. This is the reason for the proposal of a *mix-norm* by Mathew et al [93, 94], which defines a variance-like quantity in which the smaller length-scales are suppressed. The definition is given for spatial domains which are periodic (for example, 2D domains which are periodic in both x and y), in which a Fourier representation $c(\boldsymbol{x},t) = \sum_{\boldsymbol{k}} c_{\boldsymbol{k}}(t)e^{i2\pi(\boldsymbol{k}\cdot\boldsymbol{x})}$ is possible, where the average value of c has been subtracted already to ensure that $\langle c\rangle = 0$. For example, in the 2D case with the (spatially periodic) domain being the unit square, this involves summations over the wavenumber $\boldsymbol{k} = (k_x, k_y)$, where $k_x \in \{0, \pm 1, \pm 2, \cdots\}$ and similarly for k_y. Then, the mix-norm is equivalent to the Sobolev $H^{-1/2}$ norm, and is given by [93, 94]

$$\sigma_m(t) := \left(\sum_{\boldsymbol{k}} \frac{\left|c_{\boldsymbol{k}}(t)\right|^2}{\left(1 + 4\pi^2\left|\boldsymbol{k}\right|^2\right)^{1/2}}\right)^{1/2}. \tag{4}$$

The intuition is that the smaller length-scales (larger wavenumbers) are given less prominence in the calculation (should the denominator above be unity, this is equivalent to the variance; the mix-norm therefore weights each length-scale differently in order to obtain a fuller picture of the concentration). Non-periodic domains require more complicated definitions, which makes the mix-norm difficult to use. However, the mix-norm (and its closely-related forms [82, 95]) are useful in the appropriate geometries, and also have theoretical utility for optimizing mixing [82, 93–96].

2.4. Capturing stretching of fluid blobs: Lyapunov exponents

When the velocity $\boldsymbol{v}$ is known, an alternative measure which in some senses quantifies mixing is the Finite-Time Lyapunov Exponent (FTLE). This is quite different from the concentration variance measures in that it is not the mixing of a concentration that is evaluated, but rather the stretching of fluid blobs. Lyapunov exponents are commonly cited as measuring the 'chaotic mixing' in flows, but in reality measure the relative deformation of a fluid particle in relation to nearby particles, over a given finite time interval (say from $t = 0$ to $t = T$). Suppose the particle of interest is located at $\boldsymbol{x}_0$ at time 0. This particle, and particles near to $\boldsymbol{x}_0$ in all directions, are advected by $\boldsymbol{v}$ according to (1) for this time duration. The nearby particle which has experienced the *most* separation from the main particle is then identified, and this amount of the separation, after a suitable logarithmic scaling, is characterized as the Finite-Time Lyapunov Exponent (FTLE) of the location $\boldsymbol{x}_0$. This process is carried out for all locations in a spatial grid, thereby generating a scalar field. In 2D, for example, this can be viewed

as a color map, in which high regions of fluid blob deformation will be visible as those with high FTLE values. Thus, this process generates not just one global number for 'mixing,' but a scalar field from which the regions experiencing higher 'mixing' than others can be identified. (The relationship to chaotic mixing arises from the fact that ridges of the FTLE field are associated with stable and unstable manifolds whose intersections—as shall be described subsequently—are associated with chaotic transport.)

FTLEs, and closely related measures, are experiencing extensive interest in fluid mixing problems at the laboratory [91, 97–99, e.g.] and geophysical [100–105, e.g.] scales. Since computing the FTLE at each location requires advecting many nearby particles, obtaining a refined FTLE field can be computationally expensive. Thus, there are many ongoing studies on improving the methodology of FTLE computations [101, 106, 107]. Since good spatial resolution is required for computing FTLEs, their usage in microfluidic devices has only been taken up by a few studies [26, 28, 29, 35]; this however should be no bar to their being used in DNSs of such devices.

3. Barriers to mixing

The discussion on FTLEs reveals that mixing does *not* occur homogeneously, but occurs preferentially in some regions as opposed to others. Moreover, these regions turn out to move around in space, as would be visible if FTLEs were computed at different times. For the purposes of this review, we shall think of *FTLE ridges* as codimension-1 (that is, one dimension less than the spatial dimension being considered) entities that have a sharply larger FTLE value than adjacent regions. Thus, for an experiment/simulation in 2D, the FTLE ridges will be curves, whereas for a 3D experiment they will be surfaces. FTLE ridges are regions in which particle spreading is largest, and (given the logarithmic scale of the FTLE), this usually traslates into *exponential* stretching *away from the ridge*. That is, there is a large diversion of particles that occurs near the ridge; particles on each side get pushed further away from the ridge, resulting in a quick separation between nearby particles which happen to have the ridge in between. Thus, FTLE ridges are in some senses *barriers* to fluid mixing. This might appear a paradoxical statement because of the understanding that chaotic mixing is identified by regions of large FTLE; as shall be seen, the nearby flow often exhibits complicated stretching and folding characteristics indicative of 'excellent' mixing.

3.1. Lagrangian Coherent Structures

The barriers to mixing as given by ridges of the FTLE field are more properly stated through the idea of *Lagrangian Coherent Structures* (LCSs), a term coined by Haller and collaborators [108, 109]. The observation was that in 'most' flows, there were typically structures which remained 'almost coherent,' even though they do move around in the flow. The word 'Lagrangian' in the phrase LCS for these structures is used in the fluid mechanical sense as associated with 'moving with the flow' or 'following particles' (as opposed to the 'Eulerian' viewpoint in which fluid properties are examined as a function of position and time). Typically, LCSs are surrounded by regions of larger mixing. Examples of these from geophysical flows include oceanic eddies, the Antarctic circumpolar vortex (the 'ozone hole'), and Jupiter's Great Red Spot. Similar structures exist in laboratory and microscale fluid motion as well, and represent blobs which are resistant to mixing fluid with the surroundings. Hence, understanding these entities is of importance if good mixing is desired. The key observation by Haller [108, 109] was that in order to study the LCSs, it was necessary to *follow fluid particles* (i.e., Lagrangian particle trajectories), and that information obtained from frozen-time pictures (i.e., the Eulerian viewpoint) was not necessarily correlated with these structures [110, cf.].

At this point, an issue regarding terminology must be mentioned. While the above discussion makes clear that it is the coherent *structures* which are the LCSs, in recent literature it is often the *boundaries of these structures* which are referred to as LCSs. One reason for this unfortunate terminology is that methods for locating coherent structures (described further in Section 3.2) usually focus on determining these boundaries. In *steady* flows in which there is no time-variation, the boundaries can be described in terms of classical dynamical systems theory. Consider once again Figure 1, which shows the flow patterns for several steady flows, loosely based on microfluidic situations. Each magenta curve forms a flow barriers which are interior to the fluid flow. In Figure 1(a), it forms the interface between the upper and lower fluids, which tend to flow in parallel along the channel [19–35]. In Figure 1(b), the curved barrier separates the interior of the circular microdroplet from the exterior fluid, while the interior straight barrier separates the fluid within the droplet into an upper and lower cell [10, 36–43].

What is important to note in Figure 1 is that the flow barriers are connectors between saddle-like fixed (stagnation) points. Indeed, the barrier is part of the stable manifold of a fixed point, and simultaneously part of the unstable manifold of another (possibly

the same) fixed point. Here, the *stable manifold* refers to the set of points approaching the fixed point as time progresses to infinity, while the *unstable manifold* consists of points approaching a fixed point as time goes to negative infinity. An entity which is both a stable and an unstable manifold is called a *heteroclinic manifold* or *heteroclinic trajectory*; in the special instance in which the fixed point at both ends is the same, it is called a *homoclinic manifold*. In any event, the point is that for steady flows, *heteroclinic manifolds are the important flow barriers*.

Realistic flows are however unsteady; their velocities change with time. Generically, this means that there are no fixed points. It turns out that the unsteady analogue of the saddle fixed point is called a *hyperbolic trajectory* [104, 111–113], which does *not* remain at one location, but moves around in time. Its defining characteristic is the presence of a manifold of points which get attracted to it in forwards time, and another set of points which do so in backwards time. (Defining this precisely requires the concept of *exponential dichotomies* [111, 114] which is beyond the scope of this review article.) Instantaneous stagnation points have *no* relationship to hyperbolic trajectories. This is an example of how the Eulerian (fixed-time) information is insufficient to determine Lagrangian (following the flow) information. Since the flow is unsteady, *the manifolds themselves will be moving around in time*. These are then the purported *unsteady flow barriers* of the flow, and are well-known to form a skeleton which governs transport [115]. For example, fluid cannot cross these, and there is exponential separation of particles which begin life on the two sides of such a barrier.

While this is a pleasing interpretation, there are considerable difficulties beyond the above simple statement. In the steady situation as shown in Figure 1, such manifolds are guaranteed to *not intersect* each other, except in the degenerate situation of them *coinciding*. (This is a result of the uniqueness of flow trajectories; should there be a nondegenerate intersection, fluid particles at the point of intersection do not know in which of the two directions they must travel.) However, in the unsteady situation there is no such requirement, and generically the manifolds will intersect each other in different ways. This causes difficulty in the interpretation of these manifolds as flow barriers. For example, under a time-dependent perturbation the straight flow barriers in Figure 1 would break up into a varied collection of stable and unstable manifolds of the two hyperbolic trajectories, which while being nearby the steady manifolds would not coincide with them. There would typically be a tangling between the stable and the unstable manifolds, which then means that the boudaries between the upper and lower fluids cannot be umambiguously defined. Indeed, fluid transport will occur across these (previously impermeable) barriers—so in what sense does the word 'barrier' make sense?

Typically, outside of an ill-defined region in which stable and unstable manifolds intersect, the flow remains faithful. In other words, there will be (somewhat) coherent blobs of fluid towards the middle of the upper and lower cells in the droplet, with fluid interchange occurring in the region of manifold intersections. Therefore, identifying these stable and unstable manifolds—which are the entities most often called the LCSs—is crucial to understanding the main transport mechanisms [4]. Unfortunately, doing so is not always easy. There are very few examples of exactly known stable and unstable manifolds in unsteady flows [111], and a theoretical development explicitly seeking such manifolds is difficult, though some progress has been made [116, 117]. Hence, *numerical* methods for finding these barriers has become popular.

3.2. Methods for locating barriers

Having knowledge of the velocities of the flow of a system (say, from PIV, DNS, or a simple model) by itself does not identify the flow barriers in unsteady flow situations. One needs to *flow fluid particles* according to that velocity (i.e., as given in (1), and use this information to reconstruct these structures which govern transport. There are *many* competing methods which purport to do this, and there is an ongoing debate about both the legitimacy, and the efficiency, about each of these methods.

(a) *FTLEs:* The most common and popular method is to use FTLEs [29, 35, 91, 97–105], as had already been discussed in Section 2.4. By beginning at time t and going in forward time, the FTLE field can be determined. Its ridges, *forward-time FTLE ridges*, are where the maximum separation of particles occur; these are the analogues of the stable manifolds. (The reason for this can be understood by examining particles near one of the stable manifolds in Figure 1; as time increases they approach a fixed point, but particles on the two sides are then pushed away from the fixed point in opposite directions due to the influence of the unstable manifolds, resulting in a large stretching between the particles.) By doing in backwards time, the *backwards-time FTLE ridges*, analogues for unstable manifolds, can be identified. While FTLEs are perhaps the easiest flow-barrier identifying method to describe, it is known that these sometimes falsely identify structures as being important [109].

(b) *Averages along trajectories:* A scalar field similar to FTLEs can be formed by averaging some specified scalar function (such as the speed) along finite-time trajectories which are indexed by the particle location at time 0. This field is sometimes thought of as a measure of *trajectory complexity*. It has been observed that the ridges of this scalar field often match well with flow barriers obtained from other methods [118, 119], and this method has been used in applications [120–122]. A criticism leveled against these averaging methods is that they are frame-dependent [109]; a counter-argument is that in applications, the fluid mixing is to be quantified precisely in the laboratory frame of reference, and so other frames of reference are immaterial.

(c) *Transfer operator methods:* An alternative to determining ridges of scalar fields comes from the ergodic-theoretical idea of a *transfer operator* or *Perron-Frobenius operator*. In this approach, transport of a density is directly assessed by seeding many particles, allowing them to flow for a finite time, and then determining an operator which quantifies how the density of points has evolved. This operator is defined on a spatial discretization, i.e., as the transition probability from tiny spatial boxes to other spatial boxes, and can be represented by a matrix operator from the set of boxes to themselves. Suitable generalizations of the eigenvectors of this matrix, shown in a color-scale on these boxes, give an immediate spatial impression on the coherent structures, which appear as a collection of boxes of similar color. Thus, this approach directly addresses coherent structures, as opposed to their boundaries, and explicitly evaluates transport of a scalar density (i.e., a concentration). Considerable theoretical work has been done on this method [81, 123–126], with many emerging applications [127, 128] in realistic fluid-mechanical situations.

(d) *Other methods:* There are many other methods which are suggested, including curves of minimum flux [129, 130], curves of minimum curvature deformation [131], curves of extremal braiding entropy [132], extent of trajectories [133], entropy and ergodic measures [134, 135], and a range of tools continuing to be developed by Haller [109, 136–138] which explicitly characterize the most/least attracting curves. Indeed, Haller *defines* LCSs using this criterion (though the concept of 'flow barriers' used in this review article is much broader). Haller's methods utilize Eulerian information on the (instantaneous) Cauchy-Green strain tensor to reveal Lagrangian structures; in addition to flow barriers as discussed here, these also include several other flow features.

3.3. Barriers and transport

One important consideration about the methods above is that they are all *purely advective*; that is, they use the flow velocity (1) to advect particles, and do *not* use diffusion. This is in a broad sense perfectly reasonable for microfluidic flows, since the advective time-scales are much less than the diffusive time-scales in micro-devices. In the parlance of fluid mechanics, *stirring* (i.e., advection) is more important than *mixing* (i.e., diffusion) at these scales. Thus, the idea of *fluid mixing* is often associated directly with diffusion. So when determining transport barriers, does it make sense to ignore diffusion?

Definitively answering the above question is impossible, but several comments are in order. First, when forwards and backwards flow barriers intersect, since they are associated with exponential stretching, nearby fluid parcels experience substantial *stretching* and *folding* (more will be said about this in Section 4.1; these are signature properties of *chaotic mixing*). This causes filamentation of fluid parcels, and when the widths of the filaments become sufficiently small, diffusion becomes more effective. Thus, this intersection process results in an *advection-driven diffusion* process [6, 80, 82, 83], which while not explicitly stated in the methods for determining flow barriers, does enhance *mixing* (in any sense of the word). Second, there are new studies [23, 130] which explicitly use diffusion in their framework, and attempt to identify unsteady flow barriers within that context.

While the identification of flow barriers (i.e., LCSs) has had success in explaining a variety of issues in geophysical and other flows [120, 127], how one can use these to *maximize* fluid transport is a more vexing issue. Clearly, having the forwards- and backwards-time flow barriers intersecting often, and across a large region of space, improves transport. Are there ways of quantifying the resulting transport, in order to optimize mixing?

4. Cross-barrier transport

The answer lies in the fact that the 'flow barriers' in unsteady flows serve the dual-role of being transport barriers, *and* influencing transport through their intersection patterns. From the dynamical systems perspective, these are stable and unstable manifolds, but unlike in the idealized Figure 1, these do not need to coincide in *unsteady* flows. A given stable manifold at some instance in time may intersect with a given unstable manifold infinitely many times, a finite number of times, or not at all [116, 139]. Moreover, the stable and unstable manifolds are

themselves changing with time. Thus, determining the cross-barrier transport associated with *those particular* stable and unstable manifolds would appear to be ambiguous.

4.1. Time-periodic flow

The most well-known resolution to this problem comes when considering *incompressible* 2D *time-periodic* flows in which a 1D stable manifold intersects a 1D unstable manifold infinitely many times, such that *lobes* of equal areas are created through these intersections [140–142]. Under these considerable idealizations, through the ideas of *lobe dynamics* occurring near *turnstiles*, it is possible to rationalize the lobe areas as quantifiers of transport [140–142]. (Lobe areas had been suggested as transport quantifiers prior to this [143–145], but the idea of lobe dynamics explained exactly how the transport occurred.) The fact that the flow is time-periodic enables the definition of a *Poincaré map* [15, 16, 142] P_0 which maps fluid particle locations from time 0 to time T, the periodicity of the flow. Suppose P_0 has a fixed point $\boldsymbol{a}$ (i.e., $P_0(\boldsymbol{a}) = \boldsymbol{a}$) which is a saddle, characterized by the fact that the eigenvalues of the Jacobian derivative of P_0 are real and positive, with one being larger than 1 (representing a stretching direction), and the other being less than 1 (a contracting direction). The corresponding eigenvectors respectively indicate the directions in which the unstable and stable manifolds emanate from $\boldsymbol{a}$. Now, suppose there is a point $\boldsymbol{b}$ (which might be the same point as $\boldsymbol{a}$) which satisfies the identical conditions, and suppose as indicated in Figure 2(a) that the 1D unstable manifold (red) of $\boldsymbol{a}$ intersects the 1D stable manifold (green) of $\boldsymbol{b}$ infinitely often, moreover creating *lobes of equal areas*. Additionally, suppose that the intersection points are associated with *exactly two heteroclinic trajectories*; that is, a sets of points $\boldsymbol{r}_i$ such that $\lim_{i\to-\infty} |\boldsymbol{r}_i - \boldsymbol{a}| = 0$ and $\lim_{i\to\infty} |\boldsymbol{r}_i - \boldsymbol{b}| = 0$, and exactly one distinct set of points $\boldsymbol{s}_i$ which satisfy the same condition. The lobes created through these intersection points satisfy $L_{i+1} = P_0(L_i)$ and $M_{i+1} = P_0(M_i)$ for $i \in \mathbb{Z}$.

Now, define a *pseudo-separatrix* as the unstable manifold segment from $\boldsymbol{a}$ to $\boldsymbol{r}_0$, combined with the stable manifold segment from $\boldsymbol{r}_0$ to $\boldsymbol{b}$ (any of the *primary intersection points* can be chosen instead of $\boldsymbol{r}_0$; the following argument still holds). This is shown in Figure 2(b). It is clear that only lobes which cross the pseudo-separatrix under forward iteration of P_0 are M_{-1} and L_0, which respectively cross upwards and downwards to the lobes M_0 and L_1. These four lobes are called *turnstile* lobes, and are the only lobes associated with pseudo-separatrix crossing. Given that all lobes have the equal area A, A is a good measure of transport [141]. Since this transport actually occurs over a time T, the *average flux* A/T has been suggested as a more appropriate measure [70].

Under the geometric structure of Figure 2, the lobes' elongation, and eventual folding (which would be inevitable if the flow is confined, and guaranteed if $\boldsymbol{a} = \boldsymbol{b}$) can be used to *prove* chaotic mixing using the Smale-Birkhoff Theorem [15]. All fluid trajectories inside the lobe structures will exhibit complicated transport, getting pulled out and then re-entrenched into the 'tangled' region. This can be illustrated by repeatedly applying the Poincaré map, which has been illustrated in microfluidic applications in a variety of studies [14, 26, 29, 35, 91].

4.2. Time-aperiodic flow

When the flow is not time-periodic—as in most realistic microfluidic flows—a Poincaré map cannot be defined. Rationalizing the flux between a given stable and unstable manifold now requires a *continuous-time* viewpoint [116, 139]. The analogues of the saddle fixed points are now *hyperbolic trajectories* to which are attached stable and unstable manifolds. All these entities move around with time. Consider taking a *snapshot* of these at a specific time t, as shown in Figure 3(a). Many other assumptions of the lobe dynamics approach of Section 4.1 have also been relaxed in this figure: the flow may be compressible, there may be any number of intersections (or none), and lobe areas (if lobes exist) may be unequal. The

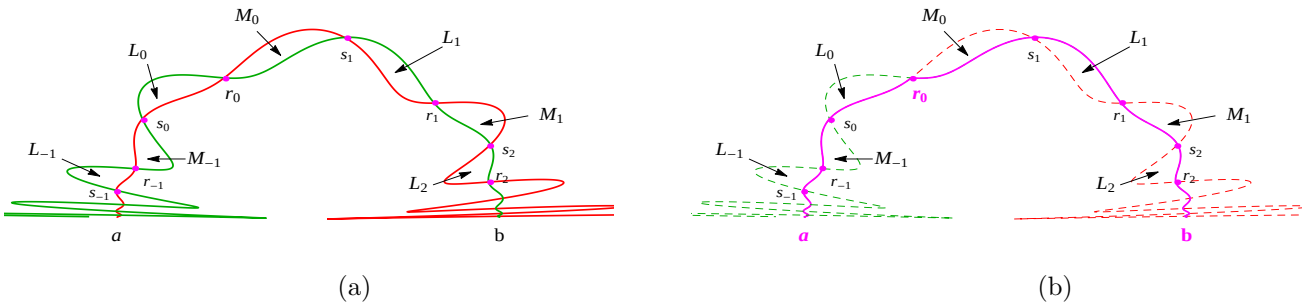

Figure 2. (a) Lobe dynamics for time-periodic flow, and (b) pseudo-separatrix (magenta).

manifolds will continue on beyond the pictured range, and may exhibit any intersection pattern in this unshown region. Consider a *fixed* line G, called a *gate surface* [139, 146, 147]. Let $\boldsymbol{u}(t)$ be the first instance in which $\boldsymbol{a}(t)$'s unstable manifold intersects G, and suppose $\boldsymbol{s}(t)$ is the closest intersection to $\boldsymbol{b}(t)$ on G of $\boldsymbol{b}(t)$'s stable manifold. Define the pseudo-separatrix at time t by the collection of curves $\boldsymbol{a}(t)-\boldsymbol{u}(t)-\boldsymbol{s}(t)-\boldsymbol{b}(t)$, as shown by the magenta curve in Figure 3(b). When the pseudo-separatrix evolves with time (with $\boldsymbol{u}(t)$ and $\boldsymbol{s}(t)$ continually redefined so as to connect between the two manifolds), the only possibility of transport across this is through the gate surface between $\boldsymbol{u}(t)$ and $\boldsymbol{s}(t)$, since the manifolds are flow barriers. Note that the portions of manifolds *beyond* the pseudo-separatrix become irrelevant in this analysis. For the picture of Figure 3(b), since the red curve is the unstable manifold and the green one is the stable manifold, flux occurs across G from left to right as shown by the heavy arrows. From the perspective of the pseudo-separatrix, this means that there is instantaneous flux transport from *below to above* the pseudo-separatrix. Let us call this a positive flux. Eventually, the intersection point to the left of G will move so that it crosses G. At that instance in time, the flux is zero. Just after this, the manifolds would have exchanged their relative positions on G, and it is clear that now the flow is in the opposite direction across the pseudo-separatrix, i.e., from above to below. The flux has therefore become negative. This evolution of the flux will continue as t is changed; if there are no manifold intersections whatsoever, the flux will be sign definite. The flux can be defined to be dimensionally consistent with an area of fluid per unit time [116, 139]. This shall be called an *instantaneous flux* [116, 139], denoted by $\phi(t)$, which quantifies the transport as the fluid per unit time occuring at each instance in time.

Incidentally, this approach can encapsulate the time-periodic Poincaré map picture, which if considered in relation to *continuous* time would have pictures like Figure 2(a) (which is associated with P_0) evolving continuously in t (i.e., with Poincaré maps P_t which map from time t to $t+T$), such that P_T is once again the same picture. However, each L_i in the time-0 picture would have been mapped to L_{i+1} in the time-T picture. Suppose G were chosen exactly at $\boldsymbol{r}_0$. If so, $\phi(0) = 0$. However, as time progresses, the intersection point $\boldsymbol{r}_0$ will move through G, and now the stable manifold will be above the unstable one, corresponding $\phi < 0$. As s_0 moves across G, ϕ will cross zero and become positive, and then at time T, r_{-1} will be exactly on G (at r_0), at which instance $\phi(T) = 0$.

Intriguingly, the instantaneous flux can also be defined in some instances where the velocities are *discontinuous*, and perhaps even *impulsive* (i.e., have infinitely large magnitudes occuring over infinitesimal times; *Dirac delta functions*) [139]. These two forms are particularly relevant if attempting to enhance mixing by respectively shaking microfluidic devices abruptly, or tapping them with an object. The potential of these situations, which incidentally have mathematical difficulties when viewed according to 'standard' dynamical systems theory, is as yet unexploited in microfluidics.

If lobes exist, their area could be obtained by

$$A = \int_{t_1}^{t_2} |\phi(t)| \, \mathrm{d}t \,, \tag{5}$$

where t_1 and t_2 are the time-values at which the end-points of the lobe cross G. This is because a lobe is created through the instantaneous flux in a fashion which is similar to that of filling a balloon through its 'mouth' G. Rom-Kedar and collaborators [140, 142] observed that, subject to the assumptions of Section 4.1, the *Melnikov function* from dynamical systems [15] could be integrated to give lobe areas in *time-periodically perturbed flows*. In time-*aperiodically* perturbed flows, and *without the additional assumptions of Section 4.1*, Balasuriya [116, 139] showed that the instantaneous flux $\phi(t)$ was *identical* to the Melnikov function, and the relationship (5) was still true.

Therefore, the instantaneous flux/Melnikov function $\phi(t)$ is an appropriate measure of cross-barrier transport in flows which have general time-dependence

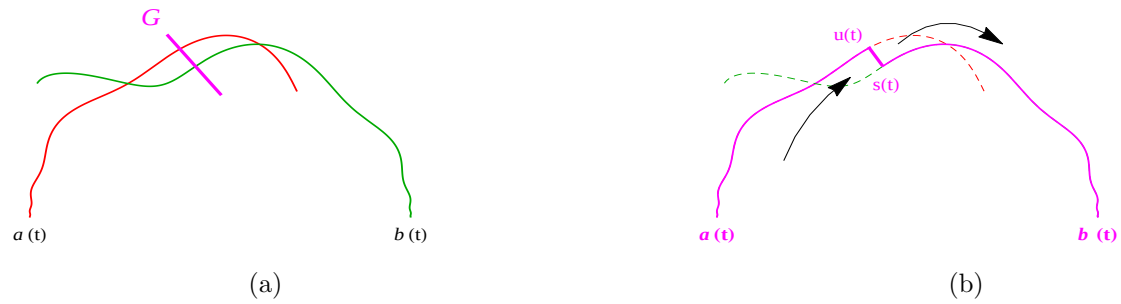

(a) (b)

Figure 3. (a) A snapshot of manifolds in time-aperiodic flow, and (b) the pseudo-separatrix (magenta) formed via the gate surface G.

in their velocity agitations. As shall be shown in Section 5, additional theory [33, 34, 71, 72, 148] applied to this fact can utilized to great advantage in *optimizing* cross-barrier transport in microfluidic designs.

4.3. Other cross-barrier transport measures

There are several other methods which have been suggested for measuring cross-barrier transport which shall be briefly mentioned. One is to define the instantaneous flux across barriers as defined by FTLE ridges [101]. Another is to provide a measure for how complicated an interface between two fluids gets as the flow evolves [31, 69, 78, 149, 150]. While this does not directly assess fluid transport, the idea is that if the interface becomes increasingly stretched and folded, then this promotes transport between the two fluids because diffusion becomes more effective. A representative description of this idea is to imagine two fluids flowing along a channel as in Figure 1(a), and to introduce one or more cross-channels which slosh fluid back and forth [31, 69]. If a dye is released on the well-defined interface to the left of these cross-channels, the evolution of the dye would give an indication of what the interface has become in the cross-channel region and beyond [31, 69, 78, 149]. This approach therefore uses the concept of *streaklines*, which combines both Lagrangian and Eulerian frameworks, in contrast to *streamlines* which are instantaneous and Eulerian, and *pathlines* which follow specific particles and are Lagrangian. (The reason the dye fills out streaklines is because it was released at one location on the flow interface.) Once these streaklines are observed, one can use some sort of folding measure [31, 69, 149, 150] as a proxy for the 'mixing' as time evolves.

5. Optimizing microfluidic cross-barrier flux

Suppose a microfluidic devices has a flow barrier—such as either of the magenta lines in Figure 1—which is a *heteroclinic manifold*. Can the various results discussed above be used to determine the velocity agitation that needs to be created (through cross-channels, microsyringes, electromagnatic forces, boundary vibration, etc) to *maximize* cross-barrier transport?

To be concrete, suppose the initial velocity field is steady, and is incompressible. Particle trajectories $\boldsymbol{x}(t)$ therefore obey

$$\frac{d\boldsymbol{x}}{dt} = J\boldsymbol{\nabla} H\left(\boldsymbol{x}\right) \quad , \quad J := \begin{pmatrix} 0 & -1 \\ 1 & 0 \end{pmatrix}, \tag{6}$$

where H is the streamfunction (or Hamiltonian). In particular, suppose $\boldsymbol{a}$ and $\boldsymbol{b}$ are saddle stagnation points of (6) connected by the heteroclinic trajectory $\bar{\boldsymbol{x}}(t)$, which forms the flow barrier Γ of interest. Since H is conserved by the flow, Γ is part of a level curve of H. To break this barrier, suppose an unsteady velocity of the specific form $\varepsilon \boldsymbol{g}(x)\cos\left(\omega t\right)$, where $0 < \varepsilon \ll 1$, is introduced. What are the 'best' choices for the spatial part of this velocity $\boldsymbol{g}(x)$ and the frequency $\omega > 0$ in order to maximize transport across the flow barrier?

For small enough ε and bounded $\boldsymbol{g}$, it is well-known [114, 117, 151, 152] that the perturbed flow

$$\frac{d\boldsymbol{x}}{dt} = J\boldsymbol{\nabla} H\left(\boldsymbol{x}\right) + \varepsilon \boldsymbol{g}\left(\boldsymbol{x}\right)\cos\left(\omega t\right) . \tag{7}$$

inherits hyperbolic trajectories $\boldsymbol{a}(t)$ and $\boldsymbol{b}(t)$ which are $\mathcal{O}(\varepsilon)$-close to $\boldsymbol{a}$ and $\boldsymbol{b}$ for all $t \in \mathbb{R}$. The trajectory $\boldsymbol{a}(t)$ retains its unstable manifold, while $\boldsymbol{b}(t)$ retains its stable manifold, and the primary segments of each are $\mathcal{O}(\varepsilon)$-close to Γ. However, these are t-dependent, and need not coincide any more; the typical picture in each t-slice is as given in Figure 3(a). It however turns out that under these conditions of time-periodicity and incompressibility, the picture is actually more special: it is exactly in the form of Figure 2(a), with the lobe areas being identical [72, 116, 148]. More can be said, by defining

$$\lambda(t) := \boldsymbol{g}\left(\bar{\boldsymbol{x}}(t)\right) \cdot \boldsymbol{\nabla} H\left(\bar{\boldsymbol{x}}(t)\right) \ , \ \Lambda(\omega) := \mathcal{F}\left\{\lambda(t)\right\}(\omega) \tag{8}$$

where $\mathcal{F}$ is the Fourier transform defined by $\mathcal{F}\left\{h(t)\right\}(k) := \int_{-\infty}^{\infty} h(\tau)e^{-ik\tau}\,\mathrm{d}\tau$. Then, the instantaneous flux function associated with a gate surface which is drawn at the point $\bar{\boldsymbol{x}}(0)$ is [72, 116, 148]

$$\phi(t) = \varepsilon\left|\Lambda(\omega)\right|\cos\left[\omega t - \mathrm{Arg}\left(\Lambda(\omega)\right)\right] + \mathcal{O}(\varepsilon^2) . \tag{9}$$

Moreover, by using (5), the area of each of the lobes is [116]

$$A = \varepsilon\frac{2\left|\Lambda(\omega)\right|}{\omega} + \mathcal{O}(\varepsilon^2) \tag{10}$$

and the average flux A/T (with the period $T = 2\pi/\omega$) is [116]

$$\frac{A}{T} = \varepsilon\frac{\left|\Lambda(\omega)\right|}{\pi} + \mathcal{O}(\varepsilon^2) . \tag{11}$$

Whether using the amplitude of the instantaneous flux or the average flux as a measure of the cross-barrier transport, it is clear that what one needs to optimize is the quantity $|\Lambda(\omega)|$.

5.1. Optimum frequency of velocity agitation

The presence of a 'best' frequency is backed by experimental [25, 28, 29, 35, 56, 61–68] and numerical [30, 62–64, 66, 69] evidence (usually obtained by laboriously testing many frequency values), and theoretical considerations [70]. The few studies which either indicate that the mixing increases [32, 153, 154] or decreases [30, 155] with frequency may well arise from sampling a non-monotonic function in a monotonic region.

The above theory is now applied to the experimental device as reported by Lee et al [35] (see also [31]), and shown in Figure 4(a). Lee et al postulate parabolic velocity profiles [30, 31] in the main channel, and in the one cross-channel which they use to obtain the velocity agitation; these are respectively $V_0\left[1-(y/W_0)^2\right]$ in the x-direction, and $V_s\left[1-(x/W_s)^2\right]\cos(\omega t)$ in the y-direction. They define the Stouhal number by $\mathrm{St} := fW_s/V_0$ where $2\pi f = \omega$ [35]. After much testing, Lee et al [35] report the St-dependence on mixing (measured in a cross-sectional place at a downstream location using a mixing index akin to (2)) in their Figure 6, whose data has been extracted and is shown in Figure 4(b) by the dots. The curve is that obtained by calculating $|\Lambda(\omega)|$. The ability of the theory, which specifically addresses cross-barrier transport, to so quickly predict a optimum Strouhal number of around 0.3, in comparison to a similar result obtained *experimentally* by assessing *global mixing downstream* [35] is quite remarkable. Early application of this method can provide good insights before spending considerable time and money fabricating potentially non-optimal devices.

The calculation of $|\Lambda(\omega)|$ as shown by the curve in Figure 4(b) is done as follows. Since the length of the main channel is much larger than the width of the side channel, one can assume that the velocity on the center-line (the flow barrier) in the region $-W_s < x < W_s$ is approximately constant when the side channel is not in operation; therefore, $\boldsymbol{\nabla} H = V_0\boldsymbol{i}$ in this region. Moreover, $\varepsilon \boldsymbol{g}(\bar{\boldsymbol{x}}(t)) = V_s\left[1-(\bar{x}(t)/W_s)^2\right]\boldsymbol{j} = V_s\left[1-(V_0 t/W_s)^2\right]\boldsymbol{j}$, since $\bar{x}(t) = V_0 t$ in this region. Now, since $\boldsymbol{g} = \boldsymbol{0}$ outside this region, $\lambda(t) = 0$ for $|t| \geq W_s/V_0$, and

$$\lambda(t) = V_0 V_s\left[1-\left(\frac{V_0 t}{W_s}\right)^2\right], \quad -\frac{W_s}{V_0} < t < \frac{W_s}{V_0}.$$

Taking the Fourier transform, simplifying, and replacing ω with $2\pi\,\mathrm{St}\,V_0/W_s$ yields

$$|\Lambda| = \left(\frac{2V_s W_s}{4\pi^3}\right)\left|\frac{\sin(2\pi\,\mathrm{St}) - 2\pi\,\mathrm{St}\,\cos(2\pi\,\mathrm{St})}{\mathrm{St}^2}\right|.$$

Now, the prefactor is irrelevant in the quest for determining the best St values, and can be ignored. The remaining term is scaled by a factor of 0.05 to enable comparison with the mixing-index scale of Lee et al [35], and plotted in Figure 4(b) as the solid curve, forming an excellent predictor of the optimal frequency of fluid sloshing to use.

Incidentally, Lee et al [35] obtain as estimate of $\mathrm{St} \approx 0.32$ using a heuristic analysis based on expectations of particle positions. The method given here can be used to obtain not only this peak, but other local flux maxima of $|\Lambda|$ which occur around $\mathrm{St} = 0.95$, 1.45, 1.97, etc, when Figure 4(b) is extended in St. Moreover, the flux measure arising from this procedure provides the amplitude of the flux, expressed directly in terms of quantity of fluid crossing the interface. The Lee et al [35] analysis captures neither of these features.

A comment on the 'zero-mixing' prediction at around $\mathrm{St} = 0.72$ in Figure 4(b) is in order. This indicates a frequency value at which the $\mathcal{O}(\varepsilon)$-flux in (9) is zero. In practise, however, the flux is unlikely to be zero because of two reasons: the $\mathcal{O}(\varepsilon^2)$ terms (which cannot be determined by the present analysis) will generically contribute, and in the experimental device, there will be additional ignored effects such as diffusion and boundary layers. This is amply illustrated by the fact that the Lee et al [35] value at $\mathrm{St} \approx 0.72$ does not appear to be zero. Nonetheless, it *is* small; plotting $|\Lambda|$ can help decide what frequencies are best avoided if optimum mixing is desired.

The above example is new to the literature, and is based on the optimal frequency analysis by Balasuriya [71], developed for parallel-flowing two-fluid scenarios as in Figure 1(a) [25, 32, 56, 62, 156, 157]. In that study, two other examples (related to multi-cross channel fluid sloshing in another experiment [32] and an electro-magnetic perturtabation) were addressed [71]. The current example, though, uses quick and dirty estimates (such as the main channel velocity not changing within the duration of the cross-channel) to compute $|\Lambda|$, illustrating that maximizing cross-barrier transport is appropriate for maximizing global mixing, and that good results are possible even with gross simplifications.

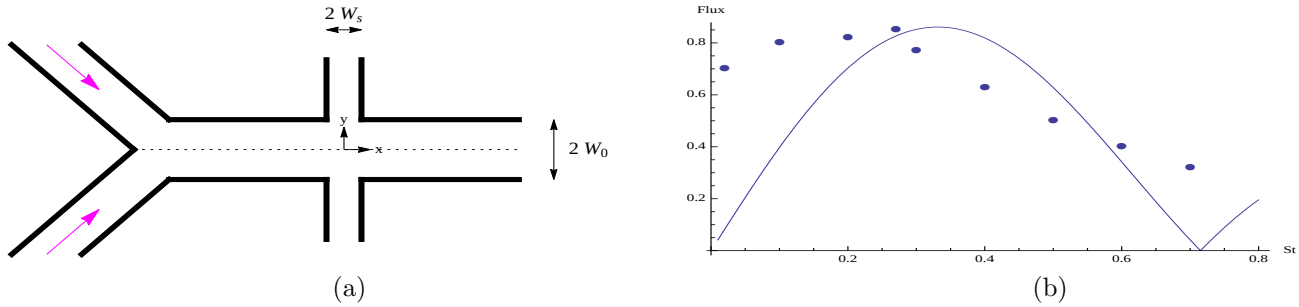

(a) (b)

Figure 4. (a) A schematic of the microfluidic device experimentally investigated by Lee et al [35], and (b) the scaled flux measure $|\Lambda|$ (solid curve) in comparison to the results of Figure 6 in [35] (dots).

5.2. Optimum positioning of velocity agitation

This section addresses the different question of whether any insight can be obtained into how *best to position the velocity agitation* spatially. For example, are there preferred locations at which to position the cross-channels in a cross-channel micromixer?

This question has been analyzed by Balasuriya through a sequence of papers [33, 34, 72] in which specific designs for cross-channel micromixers were offered [33]. For this review, attention shall be focussed only on the latest of these studies [34] which poses the problem as how to find the best positioning for a velocity agitation across the flow barrier *subject to a given energy budget*.

Under the formalism introduced in Section 5, the question is therefore to determine the best $\boldsymbol{g}(\boldsymbol{x})$. However, the results of Section 5.1 give immediate insights. Notice that the structure of the flow in the main channel was not needed in the calculations; only an estimate of the (unperturbed) velocity on the flow interface Γ. Even the postulated parabolic profile in the main channel was not used. Therefore, to leading-order, it is only necessary to consider the values of $\boldsymbol{g}$ on the flow barrier. Moreover, since $\lambda = \boldsymbol{\nabla} H \cdot \boldsymbol{g}$ and Γ is associated with a streamsurface $H =$ constant, it is only the component of $\boldsymbol{g}$ perpendicular to Γ that is useful. Hence one may as well attempt to utilize flow energies as close to Γ as possible, and in particular have this energy generate velocity agitations perpendicular to Γ.

Suppose the flow interface Γ (which may be curved) has length L, and is parametrized by arclength ℓ. Thus $\ell = 0$ and $\ell = L$ represent the beginning and ending saddle points associated with the heteroclinic connection. The question is to determine $\boldsymbol{g}$ such that the flow generated through (7) for some fixed small ε, has optimum transport across Γ, i.e., maximum $|\Lambda(\omega)|$.

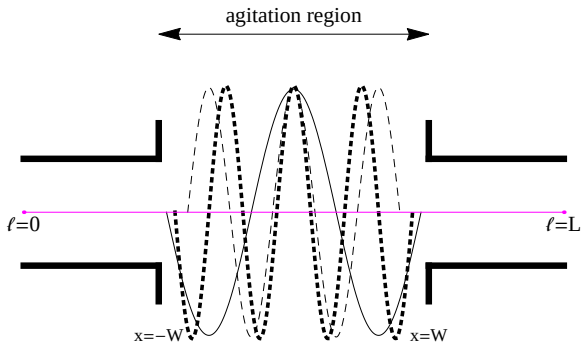

Figure 5. Optimum velocity agitation $g_\perp$ for cross-interface transport using (13) with $L = 1$, $V_0 = 1$ and $\omega = 20$ (solid profile), 40 (dashed) and 50 (dotted).

Based on the above discussion, let $g_\perp := \boldsymbol{g} \cdot \boldsymbol{\nabla} \boldsymbol{H} / |\boldsymbol{\nabla} \boldsymbol{H}|$ be the velocity orthogonal to Γ, which is subject to the kinetic energy constraint

$$\int_0^L g_\perp^2 (\ell) \, \mathrm{d}\ell = G^2 L \,, \tag{12}$$

where G is some specified constant with dimensions of velocity. Using an Euler-Lagrange variational approach, Balasuriya and Finn [34] obtain an explicit solution to this optimization problem, and demonstate its optimality through comparison of numerically computed lobe areas from other spatial forms of $\boldsymbol{g}$ which satisfy the constraint (12).

For the purposes of this review, a simple approximation which gives an easier representation than that of [34] is proposed. Consider Figure 5 in which two fluids come in from the left, and there is a central region in which some agitation strategy (cross-channels, boundary vibration, electromagnets) is to be implemented to optimize flux. This is a typical design [28–33, 69, 72, 158, 159]. The saddle points corresponding to $\ell = 0$ and $\ell = L$ are well outside this region in typical devices; at T- or Y-junctions at the inlet as in Figure 4(a), and possibly within a collecting reservoir at the outlet. Consider the simplifying assumption that the velocity along the interface *in the agitation region* in the absence of an agitation is V_0, a constant. This provided good results in the example of Section 5.1, is reasonable in most devices where the agitation region is far from saddle points, and so is worth pursuing. Suppose the midpoint of this agitation region is labeled $x = 0$, and the region itself is described by $-W < x < W$. Then, the results in [34] simplify considerably in this regime to give

$$g_\perp(x) = \frac{\sqrt{2}\, G}{\sqrt{1 + \frac{V_0}{\omega L} \sin \frac{\omega L}{V_0}}} \cos\left(\frac{\omega}{V_0} x\right) \tag{13}$$

on the flow interface for $x \in (-W, W)$. Note that $g_\perp(x) = 0$ for $|x| > W$, since no velocity agitation is used outside the region. Now, (13) tells us specifically how the perpendicular agitation velocity should vary along the interface, and it is instructive to note that it changes direction at $x_m = (2m+1)\pi V_0/(2\omega)$, where $m \in \mathbb{Z}$. To ensure continuity in the agitation, pick the largest M such that $(2M+1)\pi V_0 < 2\omega W$, and set $g_\perp$ to zero outside the region $(-x_M, x_M)$.

The results of this process are shown inside the agitation region of Figure 5 for three different choices of ω, with the other parameters being $L = 1$ and $V_0 = 1$. If examining the solid curve ($\omega = 20$), this structure of $g_\perp$ can be obtained by positioning three cross-channels adjacent to each other, with the middle one having a flow which is exactly out of phase with the outer two cross-channels. Since the velocity agitation is $\varepsilon g_\perp \cos(\omega t)$, each of these velocity profiles within the

cross-channels are modulated by $\cos\omega t$, causing fluid sloshing across this central region of Γ. The results of this theory tell us exactly where to put each of the cross-channels; their ends are located at the values x_m where $m = 0, \pm 1, \pm 2, \cdots, \pm M$. If $\omega = 40$, five cross-channels provides the optimum agitation. Moreover, it tells us to situate the cross-channels right against each other, and to have fluid flowing in opposite directions in adjacent channels. This is useful information, not hitherto used in experimental designs. Rather than using pumping in cross-channels, one could also use membranes located on the top and bottom boundaries of the agitation region [51, 52], which are made to vibrate at precisely the form given in (13), modulated by $\cos\omega t$. For example at $t = 0$, flexible upper and lower boundaries would have a deformation in the y-direction given by (13), and illustrated by the solid curve in Figure 5. By the time t has evolved to π/ω (half the period of the flow) the deformation would be negative that given in (13). When t has reached $2\pi/\omega$ they would once again be given by (13). For design purposes, it is instructive to note that boundary positions located at the x_m values will always remain stationary. These can be used to anchor the boundary membranes to the apparatus. Thinking of boundary membranes in this fashion indeed renders the energy constraint (12) much more direct: it is the energy supplied to vibrate the membranes along their length.

The method described here is considerably simplified in comparison to the original mathematical formalism [34], but has been formulated under the conditions of finding relatively easily explainable design characteristics while maintaining reasonable assumptions. It is hoped that the theoretical tools which are continuing to be developed can be adapted to satisfy these practical considerations.

5.3. Optimum channel bends for intra-droplet mixing

The methods for optimizing mixing discussed so far are active ones. A passive approach relevant to mixing within a microdroplet as shown in Figure 1(b) would be to use channel bends and/or grooves to passively create velocity agitations which influence the droplet in an unsteady fashion as it moves along the channel. The first step in this endeavour is to evaluate the role of channel boundaries on interior mixing, which has interested many authors [8, 9, 19, 27, 160]. One main issue in this process is how to precisely quantify the mixing within one particular configuration. In experimental devices [19, 27] one usually measures a variance such as (2). The difficulty in extrapolating from this is that in order to determine how changing a parameter, say the curvature of the channel, affects the mixing properties requires building yet another device. DNS modeling of this situation is also complicated by the several moving interfaces on which moving boundary conditions would need to be specified. However, simplified models [8, 48] may offer opportunities for quicker investigation of the parameter space.

In this review, the promise of a new simple model [9] will be briefly discussed. The basis for this model is the Hadamard-Rybczynski solution [8, 160–163] of a steadily translating droplet in a different medium, which specifies the velocities in the frame of reference of the microdroplet. These velocities will inevitably get modified by local channel curvature [8], but reasonable assumptions on the impact of a nearby channel boundary on the *velocity on the interior flow barrier* are possible [9]. Basically, the flow along the center of the channel must bend to keep track of how the channel boundaries are bending; additional boundary effects will of course occur, but this will only influence the droplet's interior boundary at higher-order. As has been demonstrated in several situations so far, information on the interface should be sufficient to evaluate the flux to leading-order. Of particular note is that this will avoid having to do trajectory integration and computing a global mixing measure of Section 2, as has previously been necessary even in models in which the velocity field is explicitly specified [8].

A simplification used in almost all models of

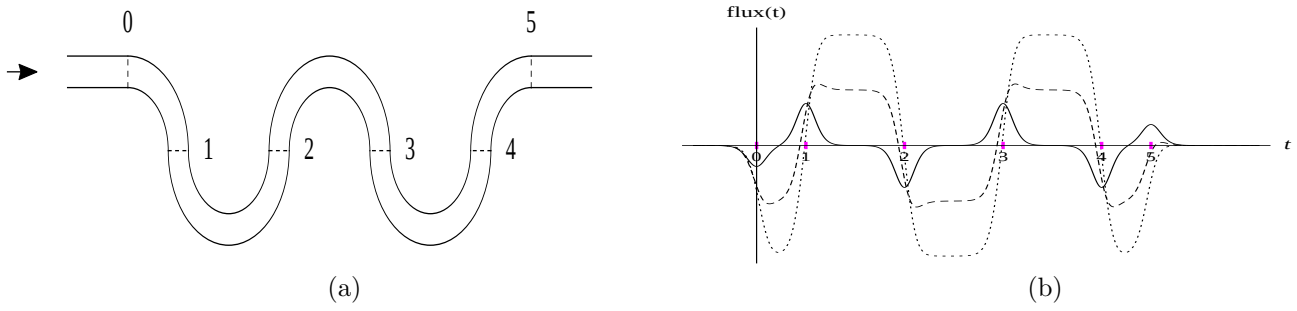

Figure 6. (a) A serpentine channel along which the microdroplet travels, and (b) resulting flux from lower to upper cell of microdroplet as a function of time.

the transport of droplets within curved channels is that the droplet *instantaneously* realigns to make sure that its axis remains parallel to the local boundaries [7, 8, 12, 40, 160]. This clearly is not reality; yet investigating this aspect has been difficult so far. As an example, Figure 6(a) shows a particular serpentine channel configuration along which a carrier fluid flows from left to right. Suppose the microdroplet travels along this channel, experiencing the local channel curvature at each instance, and reorienting towards the local channel bends *subject to a time-lag*. Note that since the bends in the channel occur only over a certain range, the droplet will experience unsteadiness in its velocities mainly over a finite time-interval; these effects will die out as time goes to $-\infty$ (at the left) and $+\infty$ (at the right). In particular, the unsteadiness experienced is *not* periodic, necessitating the aperiodic development of Section 4.2.

Figure 6(b) shows the flux function, with positivity indicating flux from the lower to the upper cell in the microdroplet picture of Figure 1(b), as a function of time t. The markers labeled 0 through 5 in Figure 6(a) are cross-sectional positions along the channel, and the same markers are given in Figure 6(b) to indicate the time-values at which the droplet is crossing those positions. While precise dimensions are not given in Figure 6 (this is the subject of a detailed article [9], which quantifies the roles of the carrier fluid velocity, viscosities of the droplet and the carrier fluids, droplet radius, and measurements of the channel geometry), the qualitative behavior of the flux function should be apparent. The three different curves shown in Figure 6(b) are associated with no time lag (solid), a small time lag (dashed) and a larger time lag (dotted) for droplet reorientation. Thus, it is possible to determine not just the time-variation of flux as a result of channel curvature, but also the effect of the time lag. It is instructive to note that the amplitude of the flux functions is highly sensitive to the time lag, pinpointing the necessity of investigating this issue in experimental and DNS processes rather than ignoring it, as is the norm.

It is hoped that this new approach—for which the time-aperiodic flux definition was essential—will provide methods for assessing the intra-droplet transport as a time-varying entity, which can be quickly computed for differing channel boundaries. This will provide a tool for more efficiently investigating the influence of how best to choose channel boundary curvature to optimize mixing within a microdroplet such as that of Figure 1(b).

5.4. Other optimizing methods

Dynamical systems inspired mixing optimization methods which are quite different from those discussed here have also been developed [93, 95, 96]. These methods impose periodic boundary conditions, and require adjusting the velocity field across the flow domain, which at this point in time renders them difficult to apply to microfluidic situations. A different class of methods attempts to control stable and unstable manifolds [164], possibly by controling the locations of hyperbolic trajectories [112, 113] to which particles on the manifolds are attracted/repulsed. The control of the direction of emanation of the manifolds from the hyperbolic trajectories has also recently been managed [165]. These methods may offer promise in the future, since by controling the stable and unstable manifolds themselves (and not just their relative location, which is all that is needed for the time-aperiodic flux quantification of Section 4.2) transport characteristics may be better optimized.

This review article has discussed the state-of-the-art in how dynamical systems methods can be used to quantify and enhance mixing in microfluidic devices. The continuing development of dynamical systems theory will indubitably provide interesting and fruitful ideas in this endeavour, into the future.

Acknowledgments

Support from the Australian Research Council through grant FT130100484 is gratefully acknowledged.

References

[1] Tabeling P 2014 *Current Opinion Biotech.* **25** 129–134

[2] Aref H 1984 *J. Fluid Mech.* **143** 1–21

[3] Aref H and et al 2015 *submitted* arXiv:1403.2953

[4] Ottino J 1990 *Annu. Rev. Fluid Mech.* **22** 207–253

[5] Whitesides G 2006 *Nature* **442** 368–373

[6] Giona M, Anderson P and Garofalo F 2013 *Phys. Rev. E* **87** 063011

[7] Chabreyrie R, Vainchtein D, Chandre C, Singh P and Aubry N 2008 *Phys. Rev. E* **77** 036314

[8] Stone Z and Stone H 2005 *Phys. Fluids* **17** 06313

[9] Balasuriya S 2015 *Phys. Fluids* submitted

[10] Grigoriev R, Schatz M and Sharma V 2006 *Lab Chip* **6** 1369–1372

[11] Kroujiline D and Stone H 1999 *Phys. D* **130** 105–132

[12] Sivasamy J, Che Z, Wong T, Nguyen N T and Yobas L 2010 *Chem. Engin. Sci.* **65** 5382–5391

[13] Che Z, Wong T and Nguyen N T 2010 *Intern. J. Heat Mass Transfer* **53** 1977–1985

[14] Che Z, Nguyen N T and Wong T 2011 *Phys. Rev. E* **84** 066309

[15] Guckenheimer J and Holmes P 1983 *Nonlinear Oscillations, Dynamical Systems and Bifurcations of Vector Fields* (New York: Springer)

[16] Alligood K, Sauer T and Yorke J 1996 *Chaos: An Introduction to Dynamical Systems* (New York: Springer)

[17] Arnold V 1965 *C. R. Acad. Sci. Paris* **261** 17–20

[18] Balasuriya S, Mezić I and Jones C 2003 *Phys. D* **176** 82–106

[19] Parsa M and Hormozi F 2014 *J. Micromech. Microeng.* **24** 065018

[20] Alam A, Afzal A and Kim K Y 2014 *Chem. Engin. Res. Design* **92** 423–434

[21] Wu C Y and Tsai R T 2013 *Chem. Engin. J.* **217** 320–328

[22] Ansari M, Kim K Y, Anwar K and Kim S 2010 *J. Micromech. Microeng.* **20** 055007

[23] Wang G, Yang F and Zhao W 2014 *Lab Chip* **14** 1452–1458

[24] Cortez-Quiroz C, Azarbadegan A, Zangeneh M and Goto A 2010 *Chem. Engin. J.* **160** 852–864

[25] Song H, Cai Z, Noh H and Bennett D 2010 *Lab Chip* **10** 734–740

[26] Park J, Seo K and Kwon T 2010 *J. Micromech. Microeng.* **20** 015023

[27] Lee D and Chen Y 2011 *AIChE J* **57** 571–580

[28] Niu X, Liu L, Wen W and Sheng P 2006 *Phys. Rev. Lett.* **97** 044501

[29] Niu X and Lee Y K 2003 *J. Micromech. Microeng.* **13** 454–462

[30] Niu X, Liu L, Wen W and Sheng P 2006 *Appl. Phys. Lett.* **88** 153508

[31] Tabeling P, Chabart M, Dodge A, Jullien C and Okkels F 2004 *Phil. Trans. R. Soc. Lond. A* **362** 987–1000

[32] Bottausci F, Cardonne C, Meinhart C and Mezić I 2007 *Lab Chip* **7** 396–398

[33] Balasuriya S 2005 *Phys. Fluids* **17** 118103

[34] Balasuriya S and Finn M 2012 *Phys. Rev. Lett.* **108** 244503

[35] Lee Y K, Shih C, Tabeling P and Ho C M 2007 *J. Fluid Mech.* **575** 425–448

[36] Frenz L, Harrack A E, Pauly M, Bégin-Colin S, Griffiths D and Baret J C 2008 *Angew. Chem. Int. Ed.* **47** 6817–6820

[37] Song H, Tice J and Ismagilov R 2003 *Angew. Chem. Int. Ed.* **42** 768–772

[38] Song H, Bringer M, Tice J, Gerdts C and Ismagilov R 2003 *Appl. Phys. Lett.* **83** 4664–4666

[39] Bringer M, Gerdts C, Song H, Tice J and Ismagilov R 2004 *Phil. Trans. R. Soc. Lond. A* **362** 1087–1104

[40] Grigoriev R 2005 *Phys. Fluids* **17** 033601

[41] Tung K Y, Li C C and Yang J T 2009 *Microfluid. Nanofluid.* **7** 545–557

[42] Cordero M, Rolfsnes H, Burnham D, Campbell P, McGloin D and Baroud C 2009 *New J. Phys.* **11** 075033

[43] Liu Z, Huang Y, Jin Y and Chen Y 2010 *Microfluid. Nanofluid.* **9** 773–786

[44] Seo K and Kim D 2014 *J. Micromech. Microeng.* **24** 085001

[45] Boreyko J, Mruetusatorn P, Retterer S and Collier C 2013 *Lab Chip* **13** 1295–1301

[46] Sun X, Tang K, Smith R and Kelly R 2013 *Microfluid. Nanofluid.* **15** 117–126

[47] Grigoriev R, Schatz M and Sharma V 2006 *Lab Chip* **6** 1369–1372

[48] Mosovky B and Meiss J 2011 *SIAM J. Appl. Dyn. Sys.* **10** 35–65

[49] Zhou X, Zhou X and Zheng B 2013 *Biomicrofluidics* **7** 054116

[50] Resto P, Berthier E, Beebe D and Williams J 2012 *Lab Chip* **12** 2221–2228

[51] de Jong J, Lammertink R and Wessling M 2006 *Lab Chip* **6** 1125–1139

[52] Wang C H and Lee G B 2005 *Biosensors Bioelectronics* **21** 419–425

[53] Mishchuk N, Heldal T, Volden T, Auerswald J and Knapp H 2011 *Microfluid. Nanofluid.* **11** 675–684

[54] Woias P 2001 *Proc. SPIE* **4560** 39–52

[55] Hernandez C, Bernard Y and Razek A 2010 *Eur. Phys. J. Appl. Phys.* **51** 20101

[56] Lim C, Lam Y and Yang C 2010 *Biomicrofluidics* **4** 014101

[57] Zhang F, Daghighi Y and Li D 2011 *J. Colloid. Interface Sci.* **364** 588–593

[58] Bazant M and Squires T 2004 *Phys. Rev. Lett.* **92** 066101

[59] Adjari A 2000 *Phys. Rev. E* **61** R45–R48

[60] Hrdlicka J, Cervenka P, Pribyl M and Snita D 2011 *Phys. Rev. E* **84** 016307

[61] Okabe Y, Chen Y, Purohit R, Corn R and Lee A 2012 *Biosensors Bioelectronics* **35** 37– 43

[62] Lin C H, Fu L M and Chien Y S 2004 *Anal. Chem.* **76** 5265–5272

[63] Fu L M, Yang R J, Lin C H and Chien Y S 2005 *Electrophoresis* **5** 1814–1824

[64] Rodrigo A, Rodrigues R, Formiga N and Mota J 2006 *Chem. Eng. Comm.* **193** 743–753

[65] Shin S, Kang I and Cho Y K 2005 *J. Micromech. Microeng.* **15** 455–462

[66] Wang Y, Zhe J, Chung B and Dutta P 2008 *Microfluid Nanofluid* **4** 375–389

[67] Wang S, Jiao Z, Huang X, Yang C and Nguyen N 2009 *Microfluid Nanofluid* **6** 847–852

[68] Suzuki H, Ho C M and Kasagi N 2004 *J. Microelectromechanical Sys.* **13** 779–790

[69] Okkels F and Tabeling P 2004 *Phys. Rev. Lett.* **92** 038301

[70] Rom-Kedar V and Poje A 1999 *Phys. Fluids* **11** 2044–2057

[71] Balasuriya S 2010 *Phys. Rev. Lett.* **105** 064501

[72] Balasuriya S 2005 *Phys. D* **202** 155–176

[73] Chung C K, Lai C, Shih T, Chang E and Chen S 2013 *Micro. Nano. Lett.* **8** 567–570

[74] Teh S Y, Lin R, Hung L H and Lee A 2008 *Lab Chip* **8** 198–220

[75] Chen D, Gerdts C and Ismagilov R 2005 *J. Am. Chem. Soc.* **127** 9672–9673

[76] Muradoglu M and Stone H 2005 *Phys. Fluids* **17** 073305

[77] Dogan H, Nas S and Muradoglu M 2009 *Int. J. Multiphase Flow* **35** 1149–1158

[78] Yun S, Lim G, Kang K and Suh Y 2013 *Chem. Engin. Sci.* **104** 82–92

[79] Conlisk K and O'Connor G 2012 *Microfluid. Nanofluid.* **12** 941–951

[80] Nguyen N T and Wu Z 2005 *J. Micromech. Microeng.* **15** R1–R16

[81] Gorodetskyi O, Giona M and Anderson P 2012 *Phys. Fluids* **24** 073603

[82] Thiffeault J L 2012 *Nonlinearity* **84** R1–R44

[83] Garofalo F and Giona M 2012 *Microfluid. Nanofluid.* **12** 175–187

[84] Sarrazin F, Loubière K, Prat L, Gourdon C, Bonometti T and Magnaudet J 2006 *Am. Inst. Chem. Eng. J.* **52** 4061–4070

[85] Sarrazin F, Bonometti T, Prat L, Gourdon C and Magnaudet J 2008 *Microfluid. Nanofluid.* **5** 131–137

[86] Li Z and Ito K 2006 *The Immersed Interface Method: Numerical Solution to PDEs Involving Interfaces and Irregular Domains* (SIAM)

[87] LeVeque R and Li Z 1994 *SIAM J. Numer. Anal.* **31** 1019

[88] Wu F and Vainchtein D 2014 *Commun. Nonlinear Sci. Numer. Simulat.* **19** 67–73

[89] Stone H, Nadim A and Strogatz S 1991 *J. Fluid Mech.* **232** 629–646

[90] Finn M D, Cox S M and Byrne H M 2004 *J. Eng. Math.* **48** 129–155

[91] Chabreyrie R, Chandre C and Aubry N 2011 *Phys. Fluids* **23** 072002

[92] Danckwerts P 1952 *Appl. Sci. Res. A* **A3** 279–296

[93] Mathew G, Mezić I, Grivopoulos S, Vaidya U and Petzold L 2007 *J. Fluid Mech.* **580** 261–281

[94] Mathew G, Mezić I and Petzold L 2005 *Physica D* **211** 23–46

[95] Lin Z, Thiffeault J L and Doering C 2011 *J. Fluid Mech.* **675** 465–476

[96] Cortelezzi L, Adrover A and Giona M 2008 *J. Fluid Mech.* **597** 199–231

[97] Raben S, Ross S and Vlachos P 2014 *Experiments Fluids* **55** 1638

[98] Miron P, Vetel J and Garon A 2014 *Experiments Fluids* **55** 1814

[99] Ouellette N 2012 *C. R. Physique* **13** 866–877

[100] d'Ovidio F, Fernandez V, Hernandez-Garcia E and Lopez C 2004 *Geophys. Res. Lett.* **31** L17203

[101] Shadden S, Lekien F and Marsden J 2005 *Phys. D* **212** 271–304

[102] Liang S, Han S, Sun Z and Hu Z 2014 *J. Hydrodynamics* **26** 558–567

[103] Qi R and Xu S 2014 *Astrophys. Space Sci.* **351** 125–133

[104] Branicki M and Wiggins S 2010 *Nonlin. Proc. Geophys.* **17** 1–36

[105] Tang W, Chan P and Haller G 2010 *Chaos* **20** 017502

[106] Conti C, Rossinelli D and Koumoutsakos P 2012 *J. Comp. Phys.* **231** 2229–2244

[107] Brunton S and Rowley C 2010 *Chaos* **20** 017503

[108] Haller G and Yuan G C 2000 *Phys. D* **147** 352–370

[109] Haller G 2015 *Annu. Rev. Fluid Mech.* **47** 137–62

[110] Haller G 2005 *J. Fluid Mech.* **525** 1–26

[111] Balasuriya S 2012 *Phys. Fluids* **24** 127101

[112] Balasuriya S and Padberg-Gehle K 2013 *SIAM J. Appl. Math.* **73** 1038–1057

[113] Balasuriya S and Padberg-Gehle K 2014 *Phys. Rev. E* **90** 032903

[114] Coppel W A 1978 *Dichotomies in Stability Theory* (*Lecture Notes in Mathematics* no 629) (Berlin: Springer-Verlag)

[115] Haller G and Peacock T 2013 *Phys. Today* **66** 41–47

[116] Balasuriya S 2014 Nonautonomous flows as open dynamical sytems: characterising escape rates and time-varying boundaries *Ergodic Theory, Open Dynamics and Structures* (Springer) chap 1, pp 1–30

[117] Balasuriya S 2011 *SIAM J. Appl. Dyn. Sys.* **10** 1100–1126

[118] Mendoza C and Mancho A 2010 *Phys. Rev. Lett.* **3** 038501

[119] Mancho A, Wiggins S, Curbelo J and Mendoza C 2013 *Commun. Nonlin. Sci. Numer. Simul.* **18** 3530–3557

[120] Mezić I, Loire S, Fonoberov V and Hogan P 2010 *Science* 1194607

[121] Kelley D, Allshouse M and Ouellette N 2013 *Phys. Rev. E* **88** 013017

[122] Mendoza C, Mancho A and Wiggins S 2014 *Nonlin. Proc. Geophys.* **21** 677–689

[123] Froyland G, Gonzalez-Tokman C and Quas A 2014 *J. Comp. Dyn.* **1** 249–278

[124] Froyland G and Padberg K 2009 *Phys. D* **238** 1507–1523

[125] Froyland G 2013 *Phys. D* **250** 1–19

[126] Froyland G, Santitissadeekorn N and Monahan A 2010 *Chaos* **20** 043116

[127] Froyland G, Stuart R and van Sebille E 2014 *Chaos* **24** 033126

[128] Froyland G, Horenkamp C, Rossi V, Santitissadeekorn N and Gupta A S 2012 *Ocean Modelling* **52** 69–75

[129] Balasuriya S, Froyland G and Santitissadeekorn N 2014 *J. Math. Anal. Appl.* **409** 119–139

[130] Balasuriya S and Froyland G 2015 in preparation

[131] Ma T and Bollt E 2014 *SIAM J. Appl. Dyn. Sys.* **13** 1106–1136

[132] Allshouse M and Thiffeault J L 2012 *Phys. D* **241** 95–105

[133] Mundel R, Fredj E, Gildor H and Rom-Kedar V 2014 *Phys. Fluids* **26** 126602

[134] Froyland G and Padberg-Gehle K 2012 *Phys. D* **241** 1612–1628

[135] Budišić M and Mezić I 2012 *Phys. D* **241** 1255–69

[136] Haller G and Beron-Vera F 2012 *Phys. D* **241** 1680–1702

[137] Farazmand M and Haller G 2013 *Chaos* **15** 023101

[138] Haller G 2001 *Phys. D* **149** 248–77

[139] Balasuriya S 2006 *Nonlinearity* **19** 282–311

[140] Rom-Kedar V, Leonard A and Wiggins S 1990 *J. Fluid Mech.* **214** 347–394

[141] Rom-Kedar V and Wiggins S 1990 *Arch. Ration. Mech. Appl.* **109** 239–298

[142] Wiggins S 1992 *Chaotic Transport in Dynamical Systems* (New York: Springer-Verlag)

[143] Channon S and Lebowitz J 1980 *Annals New York Acad. Sci.* **357** 108–118

[144] MacKay R, Meiss J and Percival I 1984 *Phys. D* **13** 55–81

[145] MacKay R and Meiss J 1988 *Phys. Rev. A* **37** 4702–4706

[146] Haller G and Poje A 1998 *Phys. D* **119** 352–380

[147] Miller P, Pratt L, Helfrich K and Jones C 2002 *J. Phys. Oceanography* **32** 80–102

[148] Balasuriya S 2005 *SIAM J. Appl. Dyn. Sys.* **4** 282–311

[149] Giona M, Cerbelli S and Adrover A 2002 *Phys. Rev. Lett.* **88** 024501

[150] Muzzio F, Alvarez M, Cerbelli S, Giona M and Adrover A 2000 *Chem. Eng. Sci.* **55** 1497–1508

[151] Yi Y 1993 *J. Differential Equations* **102** 153–187

[152] Yagasaki K 2008 *Dyn. Sys.* **23** 309–331

[153] Reis N, Vicente A, Teixeira J and Mackley M 2004 *Chem. Eng. Sci.* **59** 4967–4974

[154] Ng W, Goh S, Lam Y, Yang C and Rodríguez I 2009 *Lab Chip* 802–809

[155] Sugioka H 2010 *Phys. Rev. E* **81** 036306

[156] Yan D, Yang C, Miao J, Lam Y and Huang X 2009 *Electrophoresis* **30** 3144–3152

[157] Glasgow I and Aubry N 2003 *Lab Chip* **3** 114–120

[158] Volpert M, Meinhart C, Mezić I and Dahleh M 1999 An actively controlled micromixer *Proc. Microelectromechanical Systems (MEMS), Nashville, Tennessee 1999* vol 1 (American Society of Mechanical Engineers) pp 483–487

[159] Dodge A, Jullien M C, Lee Y K, Niu X, Okkels F and Tabeling P 2004 *C. R. Physique* **5** 557–563

[160] Mosovsky B and Meiss J 2012 *SIAM J. Appl. Dyn. Sys.* **11** 1785–1816

[161] Hadamard J 1911 *C.R. Acad. Sci. Paris* **152** 1735–1738

[162] Rybczynski W 1911 *Bull. Acad. Sci. Cracovi A* 40–46

[163] Spells K 1952 *Proc. Phys. Soc. Lond. B* **65** 541–546

[164] Balasuriya S and Padberg-Gehle K 2014 *Phys. D* **276** 48–60

[165] Balasuriya S 2015 *Chaos* submitted